Diffraction by rectangular parallelepiped, hexagonal cylinder, and three-axis ellipsoid: Some analytic solutions and numerical results

Y. Takano [a,*], K.N. Liou [a], P. Yang [b]

[a] Joint Institute for Regional Earth System Science and Engineering, and Department of Atmospheric and Oceanic Sciences, University of California, Los Angeles, CA 90095, USA
[b] Department of Atmospheric Sciences, Texas A&M University, College Station, TX 77845, USA

ARTICLE INFO

ABSTRACT

Analytical solutions are presented for Fraunhofer diffraction by the following non-spherical particles: rectangular parallelepiped, hexagonal cylinder, spheroid, and three-axis ellipsoid. Using these solutions, numerical results for the diffracted intensity of these particles in specific orientations and 3-D random orientation for an ensemble of particles of the same size are presented and discussed in terms of their minima and maxima that occur in intensity patterns, which differ substantially from their spherical counterparts.

© 2012 Elsevier Ltd. All rights reserved.

1. Introduction

The theoretical development of diffraction begins with Babinet's principle, which states that the diffraction pattern in the far field, i.e., Fraunhofer diffraction, from a circular aperture is the same as that from an opaque disk or a sphere of the same radius. Babinet [1] stated the diffraction principle by citing the corona produced by water droplets in the atmosphere. Babinet's principle can take scalar and vector forms. The vector form accounts for the sign of electric and magnetic fields. However, when the product of wavenumber and diffracting particle size is larger than about 1 and scattering angles are small, the scalar Babinet principle is sufficient for analysis [2]. See diffraction by circular cylinders [3,4] for example. The condition and limitation for Fraunhofer diffraction have been discussed by Born and Wolf [5].

The diffracted images for a circular and rectangular aperture were presented by Born and Wolf [5]. Other diffracted images for polygonal apertures were also studied by Komrska [6,7] and Smith and Marsh [8]. Cai and Liou [9]

performed the computation of diffracted intensity for randomly oriented hexagonal cylinders, while Takano and Asano [10] studied diffraction phenomena produced by randomly or horizontally oriented ice crystals. Liou et al. [11] extended their numerical computations on the diffraction by hexagonal cylinders to account for cubes and parallelepipeds. Takano and Liou [12] illustrated the manner in which the diffracted intensity can be added to the reflected/refracted intensity when the phase function for ice crystals produces a delta-function transmission at the $0°$ forward scattering direction. Parviainen et al. [13] discussed the connection of vertically elliptical coronas with horizontally oriented pollens. While carrying out the computation of the Fraunhofer integral, Tränkle and Mielke [14] simulated corona patterns using elliptical shapes and produced strong brightening for birch and pine pollens. Additionally, Bi et al. [15] illustrated good agreement between the results determined from Fraunhofer diffraction and a surface-integral method for an absorbing cube. Also, Hesse et al. [16] presented polar scattering patterns of the diffracted and externally reflected intensities for a strongly absorbing cube.

In this paper, we have applied Babinet's principle to a number of shapes, including rectangle, hexagonal cylinder, rectangular parallelepiped, spheroid, and three-axis ellipsoid to derive analytical solutions for the respective diffraction

* Corresponding author. Tel.: +1 310 794 9832; fax: +1 310 794 9796.
E-mail address: ytakano@atmos.ucla.edu (Y. Takano).

intensities. Additionally, we have also presented some pertinent computational results and discussed the physical features that occur in the diffraction patterns for single orientations as well as for 3-D random orientation involving a group of particles of the same size. In Section 2, the analytical solutions are derived for Fraunhofer diffraction involving the following shapes: rectangular parallelepiped, hexagonal cylinder, spheroid, and three-axis ellipsoid. Interpretation and discussion of the diffracted intensity follow in Section 3. Concluding remarks are given in Section 4.

2. Analytical solutions

2.1. Sphere

For reference purposes, we shall begin with a discussion on diffraction by a sphere. In the far field, the light-wave disturbance can be derived from the Fraunhofer diffraction theory following Born and Wolf [5] as follows:

$$u_p(sphere) = u_c e^{-kr_0} \iint_{A_c} \exp[-ik(x\cos\phi + y\sin\phi)\sin\theta]\,dx\,dy, \quad (1)$$

where for simplicity of presentation, we let $u_c = -iu_0/r\lambda$, where u_0 represents the disturbance in the original wave, $k = 2\pi/\lambda$, λ is the wavelength, r_0 is the distance between a diffracting particle and an observing point, A_c is the geometrical cross section area of the particle perpendicular to the incident light beam, θ is the scattering angle, and ϕ is the azimuthal angle. For a circular aperture, we can transfer the rectangular coordinates (x, y) to the polar coordinates (ρ, ψ) such that $x = \rho\cos\psi$ and $y = \rho\sin\psi$ to obtain

$$u_p = u_c e^{-ikr_0} \int_0^a \int_0^{2\pi} \exp[-ik\rho\cos(\psi - \phi)\sin\theta]\rho\,d\rho\,d\psi. \quad (2)$$

By noting the zero-order (J_0) and first-order (J_1) Bessel functions and their recurrence relationship [17], Eq. (2) can be expressed by

$$u_p = 2u_c e^{-ikr_0} A_c J_1(x\sin\theta)/x\sin\theta, \quad (3)$$

where the geometric shadow area $A_c = \pi a^2$, $y = x\sin\theta$, and the size parameter $x = ka$. The scattered intensity in terms of the incident intensity $I_0 = |u_0|^2$ can then be written in the form

$$I_d = |u_p|^2 = I_0 \frac{i_p}{k^2 r^2} \quad \text{where } i_p(\theta; ka) = \frac{x^4}{4}[2J_1(y)/y]^2. \quad (4)$$

2.2. Rectangular parallelepiped

Consider a plane wave incident on a rectangular parallelepiped from a direction with a zenith angle $(\pi/2 - \alpha)$ and an azimuthal angle β measured with respect to the coordinate system fixed to the parallelepiped, as shown in Fig. 1a,
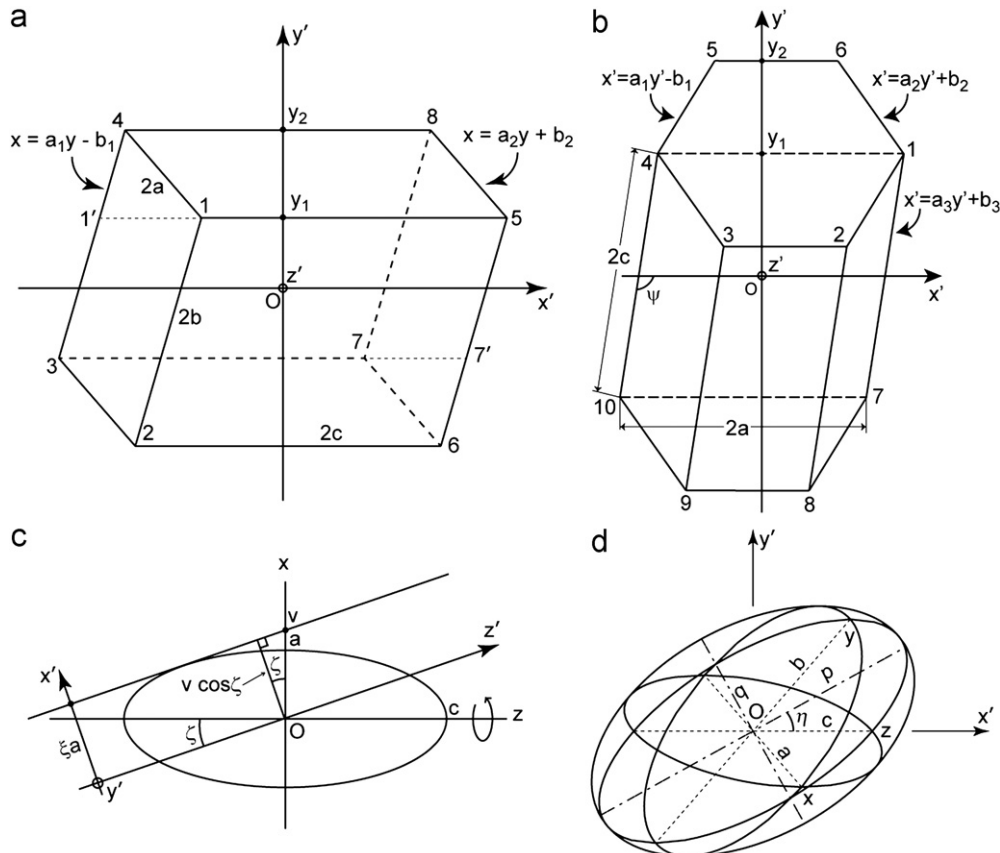
Fig. 1. Geometric shadow of (a) a rectangular parallelepiped, (b) a hexagonal cylinder, and (d) a three-axis ellipsoid projected on a plane normal to an incident direction. (c) Geometry showing semi-major axis of shadow ellipse of a spheroid projected on a plane normal to an incident direction.

where the x-, y-, and z-axes are directed, respectively, through the centers of three sets of rectangular planes. The origin O of the coordinate system is taken at the center of the parallelepiped. The geometric shadow of the parallelepiped projected onto a plane normal to the incident direction is expressed in terms of the (x', y') coordinates of its marginal vertexes in a new coordinate system, where the z'-axis is taken along the incident direction (see Fig. 1a). The transformation of the body-framed coordinate system $\mathbf{X}(x, y, z)$ into the new coordinate system $\mathbf{X}'(x', y', z')$ can be written in the form

$$\mathbf{X}' = \mathbf{CDX}, \tag{5}$$

where the transformation matrices are given by

$$\mathbf{C} = \begin{bmatrix} \sin\alpha & 0 & -\cos\alpha \\ 0 & 1 & 0 \\ \cos\alpha & 0 & \sin\alpha \end{bmatrix}, \tag{6}$$

$$\mathbf{D} = \begin{bmatrix} \cos\beta & \sin\beta & 0 \\ -\sin\beta & \cos\beta & 0 \\ 0 & 0 & 1 \end{bmatrix}. \tag{7}$$

Thus, if the size and shape of the parallelepiped and the propagation direction (α,β) of the incident wave are known, the coefficients a_1, a_2, b_1, b_2, y_1, and y_2 defined in Fig. 1a can be determined by Eq. (5).

The shape of a parallelepiped is defined by the lengths a, b, and c, which are half lengths of a rectangular parallelepiped along the three axes with the size parameter given by ka. Having defined these geometric variables, we may rewrite the integral equation denoted in Eq. (1) in the form

$$u_p(parallelepiped) = u_c e^{-ikr_0} \iint_{A_p} \exp[-i(Xx' + Yy')]dx'\,dy', \tag{8}$$

where

$$\left.\begin{array}{l} X = k\sin\theta\cos\phi, \\ Y = k\sin\theta\sin\phi. \end{array}\right\} \tag{9}$$

The integration of Eq. (8) over the geometric shadow area bounded by (2–3–4–8–5–6–2), shown in Fig. 1a, can be performed by dividing the whole integration domain into three sub-domains: two trapezoids (1′–4–8–5–1′) and (3–7′–6–2–3) and one parallelogram (1′–5–7′–3–1′). In this manner, we can use the integration method developed by Smith and Marsh [8] to carry out these integrations. It follows that the diffraction amplitude $u_p/u_c e^{-ikr_0}$ of a parallelepiped defined by the orientation position (α,β) at an arbitrary point $P(\theta,\varphi)$ can be obtained in the form

$$u_p(\theta,\phi;\alpha,\beta;ka,b/a,c/a)/u_c e^{-ikr_0}$$

$$= \frac{4}{X(a_1X+Y)}\sin\left[\frac{1}{2}(y_2-y_1)(a_1X+Y)\right]$$

$$\sin\left\{\frac{1}{2}\left[-a_1(y_1-y_2)+2b_1\right]X-\frac{1}{2}(y_1+y_2)\right\}$$

$$+ \frac{4}{X(a_2X+Y)}\sin\left[\frac{1}{2}(y_2-y_1)(a_2X+Y)\right]$$

$$\sin\left\{\frac{1}{2}\left[a_2(y_1+y_2)+2b_2\right]X+\frac{1}{2}(y_1+y_2)\right\}$$

$$+ \frac{4}{X(a_1X+Y)}\sin[y_1(a_1X+Y)]\sin(b_1X), \tag{10}$$

where a_1, a_2, b_1, b_2, y_1, and y_2 are given explicitly as functions of α, β, a, b, and c as follows:

$$a_1 = \sin\alpha\tan\beta, \tag{11}$$

$$a_2 = -\sin\alpha/\tan\beta, \tag{12}$$

$$\begin{aligned} b_1 = \sin\alpha\tan\beta(a\sin\beta - b\cos\beta) + a\sin\alpha\cos\beta \\ + b\sin\alpha\sin\beta + c\cos\alpha, \end{aligned} \tag{13}$$

$$\begin{aligned} b_2 = -(\sin\alpha/\tan\beta)(a\sin\beta - b\cos\beta) + a\sin\alpha\cos\beta \\ + b\sin\alpha\sin\beta + c\cos\alpha, \end{aligned} \tag{14}$$

$$y_1 = -a\sin\beta + b\cos\beta, \tag{15}$$

$$y_2 = a\sin\beta + b\cos\beta. \tag{16}$$

It follows that the intensity function for a given orientation of a rectangular parallelepiped defined by angles α and β is given by

$$i_p(\theta,\phi;\alpha,\beta;ka,b/a,c/a) = \left(\frac{k^2}{2\pi}\right)^2 \left|u_p/u_c e^{-ikr_0}\right|^2. \tag{17}$$

For application to a rectangular aperture, we can define the geometric shadow area as $2aL$, where $2a$ and L are the lengths of a rectangle. In reference to Eq. (1), we may let the integrating boundaries x and y be from $-a$ to a and from $-L/2$ to $L/2$, respectively. A separation of the two integrations leads to

$$u_p(rectangle) = u_c e^{-kr_0} \int_{-a}^{a} \exp(-ikx\cos\phi\sin\theta)dx$$

$$\times \int_{-L/2}^{L/2} \exp(-iky\sin\phi\sin\theta)dy$$

$$= u_c e^{-kr_0} 4a(L/2)\frac{\sin(ka\cos\phi\sin\theta)}{ka\cos\phi\sin\theta}\frac{\sin[k(L/2)\sin\phi\sin\theta]}{k(L/2)\sin\phi\sin\theta}. \tag{18}$$

The solution of diffraction due to the light wave disturbance associated with a rectangle in the far field is given by the product of sine functions. It follows that the intensity function for diffraction can be expressed by

$$i_p[\theta,\phi;ka,k(L/2)] = \frac{4k^4a^2(L/2)^2}{\pi^2}$$

$$\frac{\sin^2(ka\cos\phi\sin\theta)}{(ka\cos\phi\sin\theta)^2}\frac{\sin^2[k(L/2)\sin\phi\sin\theta]}{[k(L/2)\sin\phi\sin\theta]^2}. \tag{19}$$

If we set that $\alpha=0$, $\beta=0$, $b=a$, and $c=L/2$ in Eq. (10), Eq. (17) reduces to Eq. (19) as a special case.

2.3. Hexagonal cylinder

Procedures for the determination of the diffraction by a hexagonal cylinder have been described by Takano and Asano [10]. They are similar to the rectangular parallelepiped case presented above. However, an additional matrix $\mathbf{B}$ must be applied to $\mathbf{X}$ in order for the bases of trapezoids to be parallel to the x'-axis, as shown in Fig. 1b, in the form

$$\mathbf{X}' = \mathbf{BCDX}, \tag{20}$$

where the transformation matrix is given by

$$\mathbf{B} = \begin{bmatrix} \cos\psi & \sin\psi & 0 \\ -\sin\psi & \cos\psi & 0 \\ 0 & 0 & 1 \end{bmatrix}. \tag{21}$$

The relationship among the three angles is defined by the following equation:

$$\tan\psi = -\tan\left(\beta + \frac{\pi}{3}\right) / \sin\alpha, \quad (0 \le \psi \le \pi). \tag{22}$$

It follows that the diffraction amplitude of a hexagonal cylinder defined by the orientation position (α, β) at an arbitrary point $P(\theta, \phi)$ can be obtained in the form

$$
u_p(\theta,\phi;\alpha,\beta;ka,c/a)/u_c e^{-ikr_0}
$$
$$
= \frac{4}{X(a_1X+Y)}\sin\left[\frac{1}{2}(y_2-y_1)(a_1X+Y)\right]
$$
$$
\sin\left\{\frac{1}{2}\left[-a_1(y_1-y_2)+2b_1\right]X - \frac{1}{2}(y_1+y_2)\right\}
$$
$$
+ \frac{4}{X(a_2X+Y)}\sin\left[\frac{1}{2}(y_2-y_1)(a_2X+Y)\right]
$$
$$
\sin\left\{\frac{1}{2}\left[a_2(y_1+y_2)+2b_2\right]X + \frac{1}{2}(y_1+y_2)\right\}
$$
$$
+ \frac{4}{X(a_3X+Y)}\sin[y_1(a_3X+Y)]\sin(b_3X). \tag{23}
$$

Note that a_1, a_2, a_3, b_1, b_2, b_3, y_1, and y_2 defined in Fig. 1b are not expressed explicitly in terms of the variables α, β, a, and c which differ from the rectangular parallelepiped case.

2.4. Spheroid

The geometric shadow of a spheroid projected onto a plane perpendicular to the incident direction is generally an ellipse. We can specify an orientation of a spheroid by an angle ζ ($=\pi/2-\alpha$) between the incident direction and its rotation axis. An ellipse can be defined as a circle with a radius a multiplied by a factor ξ in the direction Ox' (Fig. 1c). Thus, the elliptical aperture A_e is equal to a circular aperture A_c multiplied by ξ in the direction Ox'. In reference to Eq. (1) and by changing variables such that $x'=x/\xi$ and $y'=y$, we obtain

$$
u_p(spheroid) = \xi u_c e^{-ikr_0} \iint_{A_c} \exp[-ik(x'\xi\cos\phi \\ + y'\sin\phi)\sin\theta]dx'\,dy'. \tag{24}
$$

We may transfer the rectangular coordinate (x',y') to the polar coordinate (ρ,ψ) such that $x' = \rho\cos\psi$ and $y' = \rho\sin\psi$. In this manner, Eq. (24) can be rewritten as follows:

$$
u_p = \xi u_c e^{-ikr_0} \int_0^a \int_0^{2\pi} \exp[-k\rho l\cos(\psi-\sigma)\sin\theta]\rho\,d\rho\,d\psi, \tag{25}
$$

where $\sigma = \tan^{-1}(\tan\phi/\xi)$, $l = (\xi^2\cos^2\phi + \sin^2\phi)^{1/2}$, and $\xi = [(c/a)^2\sin^2\zeta + \cos^2\zeta]^{1/2}$, which is derived below. In terms of the zero-order Bessel function, we have

$$
u_p = \xi u_c e^{-ikr_0} 2\pi \int_0^a J_0(k\rho l\sin\theta)\rho\,d\rho. \tag{26}
$$

Using the relationship between the zero- and first-order Bessel functions and from Eq. (26), we can show that

$$
u_p = u_c e^{-ikr_0} A_e \frac{2J_1(xl\sin\theta)}{xl\sin\theta}, \tag{27}
$$

where the geometric shadow area $A_e = \xi\pi a^2$ and the size parameter $x = ka$. On using Eq. (17), the intensity function for diffraction by a spheroid can be expressed in the form:

$$
i_p(\theta,\phi;\zeta;ka,c/a) = \frac{\xi^2 x^4}{4}\left[\frac{2J_1(lx\sin\theta)}{lx\sin\theta}\right]^2. \tag{28}
$$

Note that the spheroid and the incident light beam are defined by the following two equations:

$$
\frac{x^2}{a^2} + \frac{z^2}{c^2} = 1, \tag{29a}
$$

$$
x = \tan\zeta z + \nu, \tag{29b}
$$

where the intercept ν is still unknown, but can be determined by substituting Eq. (29b) into Eq. (29a) to yield

$$
\left(\frac{1}{c^2} + \frac{\tan^2\zeta}{a^2}\right)z^2 + \frac{2\nu\tan\zeta}{a^2}z + \frac{\nu^2}{a^2} - 1 = 0. \tag{30}
$$

In order to have the incident beam tangent to the spheroid, a discriminant D' must be 0 such that

$$
D' = \left(\frac{\nu\tan\zeta}{a^2}\right)^2 - \left(\frac{1}{c^2} + \frac{\tan^2\zeta}{a^2}\right)\left(\frac{\nu^2}{a^2} - 1\right) = 0, \tag{31}
$$

which leads to the solution in the form: $\nu = \pm(c^2\tan^2\zeta + a^2)^{1/2}$. From Fig. 1c, we find the following relationship:

$$
\xi a = |\nu|\cos\zeta = a[(c/a)^2\sin^2\zeta + \cos^2\zeta]^{1/2}. \tag{32}
$$

Thus, we obtain

$$
\xi = [(c/a)^2\sin^2\zeta + \cos^2\zeta]^{1/2}. \tag{33}
$$

2.5. Three-axis ellipsoid

Three-axis ellipsoid is governed by the following geometric relationship:

$$
\frac{x^2}{a^2} + \frac{y^2}{b^2} + \frac{z^2}{c^2} = 1. \tag{34}
$$

When a three-axis ellipsoid is seen from an arbitrary direction expressed by angles α and β, its shadow is an ellipse, as shown in Fig. 1d. The ellipse can be obtained as follows. On solving $\mathbf{X} = (\mathbf{CD})^T \mathbf{X}'$, the coordinate system (x, y, z) can be expressed by (x', y', z'). Substituting (x, y, z) into Eq. (34), we obtain a quadratic equation on the coordinate system $(x', y', \text{and } z')$. If a discriminant D' for the quadratic equation with respect to z' is 0, another quadratic equation on x' and y' is obtained representing a shadow ellipse. Specifically, we obtain $Ax'^2 + Bx'y' + Cy'^2 = D$. A rotation of the coordinate axes $(x'y'$ plane) by an angle $\eta(=\tan^{-1}[B/(A-C)]/2)$ reduces this equation to $x''^2/p^2 + y''^2/q^2 = 1$. Hence, its semi-axis lengths p and q, and an angle η between the p-axis and x'-axis as well as its diffracted intensity can then be computed.

Finally, for randomly oriented nonspherical particles, the intensity function (hereafter referred to as intensity) i_p

can be obtained by performing integrations over the angles α, β, and ϕ in the form:

$$i_p(\theta; ka, [b/a,]c/a)$$
$$= \frac{1}{4\pi^2} \int_0^{2\pi} \int_0^{2\pi} \int_0^{\pi} i_p(\theta,\phi; ka,[b/a,]c/a; \alpha,\beta)\cos\alpha \, d\alpha \, d\beta \, d\phi. \tag{35}$$

3. Interpretation of diffracted intensity patterns

Fig. 2 shows logarithmic contours of the intensity function for a diffracting body whose shape and orientation are defined in the inset. The wavelength used for the calculation is 0.55 μm. Any diffracted intensity would have a maximum at a scattering angle $\theta_{1st\ max}$ of 0°. Blackened portions in the figures associated with the dense contour lines depict weak diffracted intensities. The diffraction pattern of a circular aperture is concentric (Fig. 2a). It has the first and second minima at $\theta_{1st\ min}$=4.5° and $\theta_{2nd\ min}$=8.3°. These dark bands are explained by the fact that the first order Bessel function $J_1(y)$ has zeros at y=3.832 and 7.016. Fig. 2b shows the diffraction pattern of an elliptical aperture whose area is equal to that of the circle. The long-axis of an elliptical contour is along the short-axis of its aperture, such that the aspect ratio is the same as that of the aperture.

Fig. 2c is for a rectangular aperture circumscribing the ellipse in Fig. 2b. The first minimum pattern around $\theta_{1st\ max}$=0° is a rectangular shape whose aspect ratio is equal to that of the aperture but with a 90° rotation. Next to the first maximum pattern, four surrounding fans of rectangular shapes are produced. The regular hexagonal aperture produces a hexagonal pattern around $\theta_{1st\ max}$=0° surrounded by
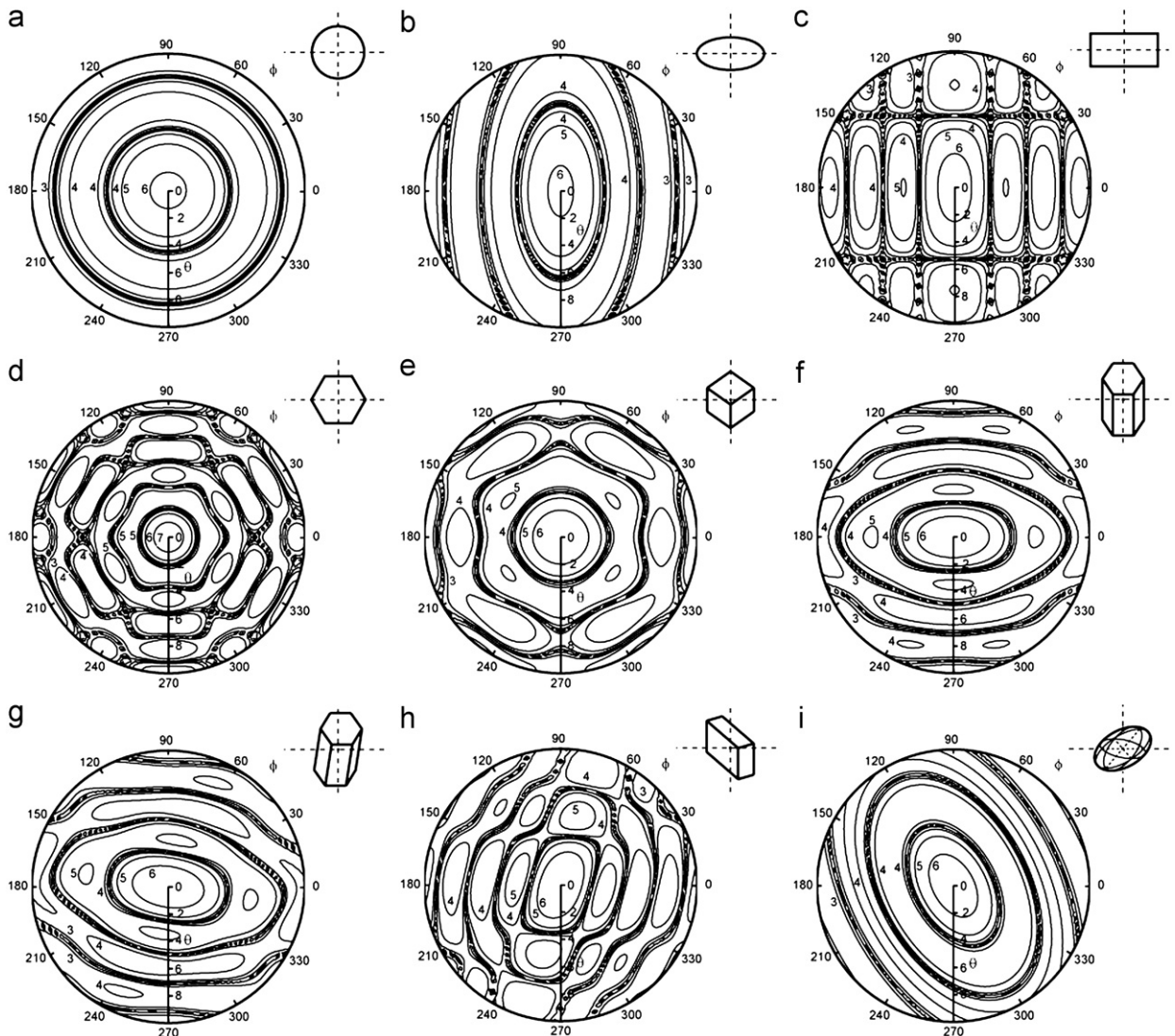
Fig. 2. Logarithmic contours of the diffracted intensity from an object whose shape and orientation are defined in the inset using a wavelength of 0.55 μm. The radial direction is the scattering angle θ from 0° to 10°. The diffracting object is (a) a circular aperture (a=4.24 μm), (b) an elliptic aperture (a=3 μm and c=6 μm), (c) a rectangular aperture (a=3 μm and $L/2$=6 μm), (d) a hexagonal aperture (a=10 μm), (e) a cube (α=45°, β=45°, and a=3.8 μm), (f) a hexagonal cylinder (α=60°, β=30°, a=4 μm, and c=8 μm), (g) a hexagonal cylinder (α=60°, β=20°, a=4 μm, and c=8 μm), (h) a rectangular parallelepiped (α=30°, β=30°, a=2 μm, b=7 μm, and c=4 μm), and (i) a three-axis ellipsoid (α=60°, β=45°, a=3 μm, b=6 μm, and c=9 μm).

six fans (Fig. 2d). However, there is a dark circle inside the hexagonal pattern, which was also shown in the work of Smith and Marsh [8]. The scattering angle $\theta_{1st\ min}$ of 2.11° at which the diffracted intensity becomes zero is identified by inspecting where the diffracted amplitude changes its sign from positive to negative. It is noted that this dark circle coincides with the first minimum of circular aperture of the same area whose radius is 9.09 μm corresponding to $y = 3.832$. The same dark circle also occurs for a regular octagonal aperture. Fig. 2e shows the diffracted pattern by a cube when light is incident obliquely. In view of the shape defined in the inset, its pattern resembles that of a hexagon but its apex has a 30° rotation. For example, there is a dark circle-like shape inside the hexagonal pattern containing the first maximum. Its approximate scattering angle θ is $\sim 3.4°$, close to the first minimum of a circular aperture of the same area which occurs at $\theta_{1st\ min} = 3.43°$.

Fig. 2f illustrates the diffraction pattern for a hexagonal cylinder for an oblique incident light beam. In view of the projected shadow in the inset, its diffraction pattern has the characteristics of both rectangular and hexagonal apertures. Fig. 2g shows another example of a hexagonal cylinder in which the incident direction in Fig. 2f is shifted by changing the rotational angle in the horizontal direction β from 30° to 20°. The diffraction pattern is also rotated by $\sim 10°$ and is not symmetric in reference to a line defined by $\phi = 90°$ and $\phi = 270°$, which differs from the pattern depicted in Fig. 2a–f. Fig. 2h is for a rectangular parallelepiped in which the shape of the projected shadow resembles a parallelogram. As a result, a parallelogram-like pattern occurs around the incident direction and is surrounded by four fans. Fig. 2i shows the diffraction pattern generated by a three-axis ellipsoid. The projected shadow is an ellipse whose semi-p-axis length is 6.6 μm, semi-q-axis length is 4.0 μm, and angle η between the p-axis axis and x-axis is 29.0°. In reference to Fig. 2b, we have shown that the diffraction pattern for an ellipse whose long axis is along the q-axis.

Fig. 3 shows the diffracted intensity for randomly oriented spheroids, hexagonal cylinders, and rectangular parallelepipeds whose aspect ratios are 4 and 1/4 (see the figure). Their cross sectional area is equal to that of a sphere with a size parameter of $ka = 100$, whose diffracted intensity is shown in the figure. The diffracted intensity corresponding to a polydisperse sphere system is also depicted for comparison purposes. To smooth out the diffracted intensity for spheres, we have used a modified gamma size distribution whose variance is 0.05. In order to interpret a series of maxima and minima generated in the diffracted intensities shown in Fig. 3, we consider the dependence of the projected shadow of a hexagonal cylinder on the angle α. In the direction of y-axis depicted in Fig. 1b when the results are averaged over the angle α and the lengths change from $\sim 2a$ to $\sim 2c$ so that the positions of maxima and minima produced by them shift resulting in a smoother average pattern. A similar interpretation can be applied to spheroids and parallelepipeds shown in the figure.

Along the x-axis direction shown in Fig. 1b, there is only one length, which is about $2a$ and is equal to $2z$. This is the characteristic length contributing to diffraction such that the maxima and minima patterns will remain even after an integration over the angle α. On the basis of Eq. (19), we may consider that the contribution of the diffracted intensity from the x-axis direction is given by $[\sin(kz\theta)/kz\theta\ ]^2$ for the preceding shapes, since a maximum intensity in the direction of $\phi = 0°$ occurs, as shown in Eq. (19). For this reason, it is anticipated that the diffracted intensity will have maxima and minima at the following angles:

$$\theta_{(n+1)\text{-th max}} = \sin^{-1}\left[\frac{(2n+1)\pi}{2kz}\right], \quad \theta_{n\text{-th min}} = \sin^{-1}\left(\frac{n\pi}{kz}\right),$$
$$n = 1, 2, 3, \dots. \tag{36}$$

Minima and maxima occur at $\theta = 4.6°$, 7.1°, and 8.0° for a prolate spheroid, as shown in the left panel of Fig. 3 corresponding to $\theta_{2nd\ max} = 4.85°$, $\theta_{2nd\ min} = 6.48°$, and θ_{3rd}
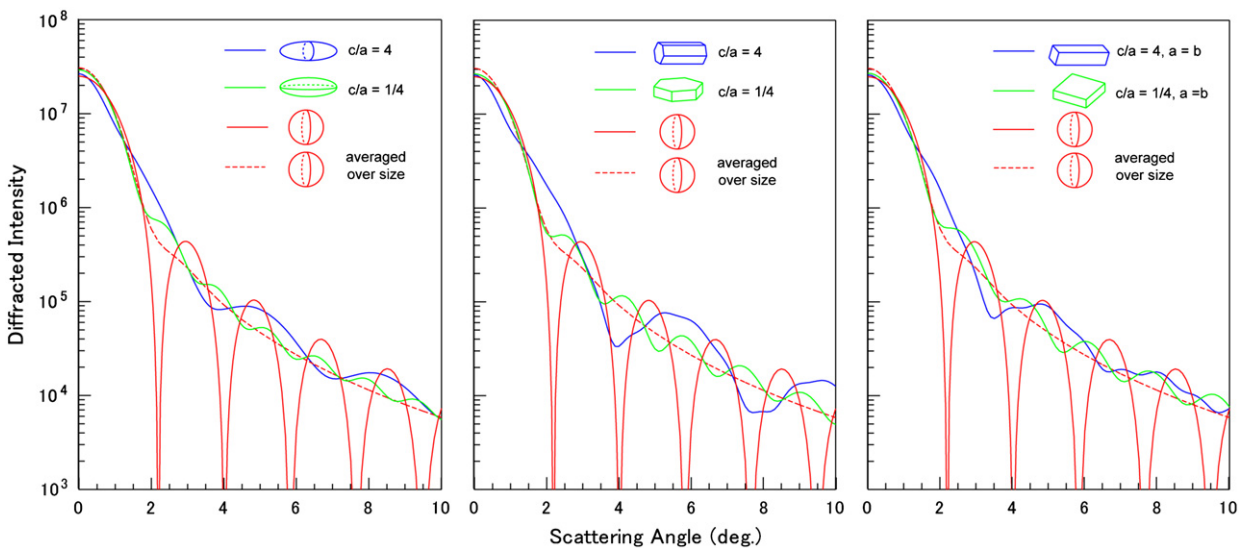

Fig. 3. Diffracted intensities for randomly oriented spheroids (left panel), hexagonal cylinders (middle panel), and rectangular parallelepipeds (right panel) defined by the aspect ratio of 4 and 1/4 using a wavelength of 0.55 μm in the calculation. Also, the diffracted intensity for an equal-area sphere with a size parameter of $ka = 100$ and the corresponding polydisperse spheres are added for comparison purposes.

$_{max}=8.11°$ by using $z=a=4.876$ μm in Eq. (36). There are minima and maxima patterns depicted at $\theta=4.7°$, $5.0°$, $6.0°$, $6.5°$, $7.4°$, $7.8°$, $8.8°$, and $9.2°$ for an oblate spheroid corresponding to $\theta_{3rd\ min}=4.07°$, $\theta_{4th\ max}=4.75°$, $\theta_{4th\ min}=5.43°$, $\theta_{5th\ max}=6.11°$, $\theta_{5th\ min}=6.79°$, $\theta_{6th\ max}=7.47°$, $\theta_{6th\ min}=8.16°$, and $\theta_{7th\ max}=8.84°$ by using $z=a=11.629$ μm in Eq. (36). Minima and maxima are illustrated at $\theta=4.0°$, $5.3°$, $7.7°$, and $9.6°$ for the hexagonal column denoted in the central panel of Fig. 3 corresponding to $\theta_{1st\ min}=3.71°$, $\theta_{2nd\ max}=5.56°$, $\theta_{2nd\ min}=7.43°$ and $\theta_{3rd\ max}=9.30°$ by employing $z=a=4.254$ μm. For a hexagonal plate, minima and maxima patterns are shown at $\theta=2.2°$, $2.4°$, $3.6°$, $4.1°$, $5.1°$, $5.7°$, $6.7°$, $7.3°$, $8.4°$, and $9.0°$ corresponding to $\theta_{1st\ min}=1.68°$, $\theta_{2nd\ max}=2.52°$, $\theta_{2nd\ min}=3.36°$, $\theta_{3rd\ max}=4.20°$, $\theta_{3rd\ min}=5.04°$, $\theta_{4th\ max}=5.89°$, $\theta_{4th\ min}=6.73°$, $\theta_{5th\ max}=7.58°$, $\theta_{5th\ min}=8.42°$, and $\theta_{6th\ max}=9.27°$ by using $z=(\sqrt{3}/2)a=9.386$ μm (radius of the inscribed circle). Minima and maxima are shown at $\theta=3.5°$, $4.8°$, $6.7°$, $8.0°$ and $9.7°$ for a columnar rectangular parallelepiped in the right panel of Fig. 3 corresponding to $\theta_{1st\ min}=3.05°$, $\theta_{2nd\ max}=4.58°$, $\theta_{2nd\ min}=6.11°$, $\theta_{3rd\ max}=7.64°$ and $\theta_{3rd\ min}=9.18°$ with a value of $z=\sqrt{2}a=5.172$ μm (radius of the circumscribed circle). There are minima and maxima at $\theta=3.8°$, $4.2°$, $5.4°$, $6.0°$, $7.1°$, $7.8°$, $8.9°$ and $9.5°$ for a planar rectangular parallelepiped, which correspond to $\theta_{2nd\ min}=3.52°$, $\theta_{3rd\ max}=4.40°$, $\theta_{3rd\ min}=5.28°$, $\theta_{4th\ max}=6.17°$, $\theta_{4th\ min}=7.05°$, $\theta_{5th\ max}=7.94°$, $\theta_{5th\ min}=8.83°$, and $\theta_{6th\ max}=9.72°$ using a value of $z=a=8.958$ μm. The diffracted intensities for polydisperse spheres are also displayed for comparison purposes.

Fig. 4 shows the diffracted intensity when the size of the diffracting particles in Fig. 3 is reduced by a factor of 1/5. Takano and Asano [10] pointed out that for the same shape, the diffracted intensity patterns for particles of different sizes are similar. The diffracted intensity for a nonspherical particle with a size ρ times larger but of the same shape can be expressed in terms of that for the

original nonspherical particle as follows:

$$i_p(\theta,\phi;\rho ka,[b/a],c/a)=\rho^4 i_p(\theta^*,\phi;ka,[b/a],c/a), \qquad (37)$$

where

$$\theta^*=\sin^{-1}(\rho\ \sin\ \theta). \qquad (38)$$

For example, $i_p\ (\theta=0)$ for a single sphere in Fig. 3 is 2.5×10^7, and $i_p(\theta=0)$ for a single sphere in Fig. 4 is $2.5\times10^7/5^4=4\times10^4$. Also, i_p (a single sphere) in Fig. 3 has the first minimum at $\theta^*=2.2°$, and i_p (a single sphere) in Fig. 4 has the first minimum at $\theta=\sin^{-1}(5\sin 2.2°)=11.1°$.

4. Concluding remarks

In this paper, we have derived analytical solutions for the diffracted intensity of a number of nonspherical particles: rectangular parallelepiped, hexagonal cylinder, spheroid, and ellipsoid. Diffraction by a three-axis ellipsoid is formulated by extending the diffraction by spheroid, although the lengths and the direction of principal axes of its shadow ellipse are computed implicitly. Numerical results on the diffracted intensity for a specific orientation of a diffracting body whose size parameter is from ~50 to ~100 as well as randomly oriented nonspherical particles whose size parameters are 20 and 100 are, respectively, displayed as contour diagrams and as a function of the scattering angle.

The results are interpreted and discussed in terms of one- and two-dimensional diffraction patterns. In the case of a hexagonal aperture, there is a dark circle within the diffracted pattern around a light source, which corresponds to a diffracted image measured by Smith and Marsh [8]. The angular radius of this dark circle coincides with that of the first minimum produced by a circular aperture of the same area as the hexagonal aperture. Finally, for randomly oriented nonspherical particles in three-dimensional space, a simple model has been
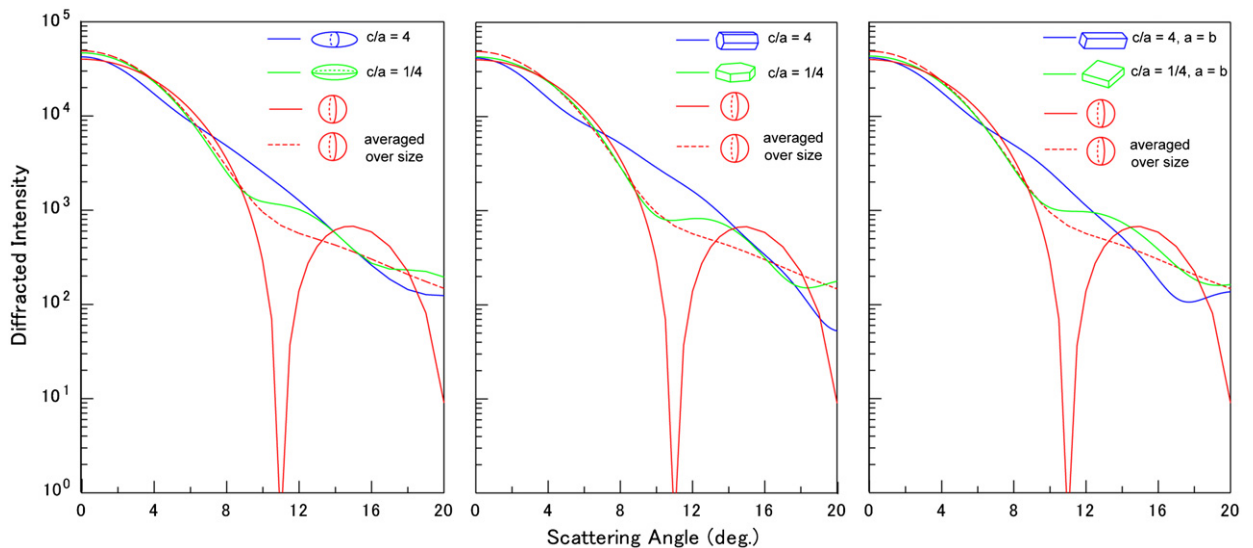

Fig. 4. Same as Fig. 3, except for $ka=20$.

developed to explain the angular positions of minima and maxima that occur in their diffracted intensity patterns.

Acknowledgments

References

[1] Babinet J. Mémoires d'optique météorologique. C R Acad Sci 1837;4:638–48.
[2] Jackson JD. Classical electrodynamics. New York: Wiley; 1975.
[3] Liou KN. Electromagnetic scattering by arbitrarily oriented ice cylinders. Appl Opt 1972;11:667–74.
[4] Takano Y, Tanaka M. Phase matrix and cross section for single scattering by circular cylinders: a comparison of ray optics and wave theory. Appl Opt 1980;19:2781–93.
[5] Born M, Wolf E. Principles of optics. Oxford: Pergamon; 1975.
[6] Komrska J. Fraunhofer diffraction at apertures in the form of regular polygons. I. Opt Acta 1972;19:807–16.
[7] Komrska J. Fraunhofer diffraction at apertures in the form of regular polygons. II. Opt Acta 1973;20:549–63.
[8] Smith RC, Marsh JS. Diffraction patterns of simple apertures. J Opt Soc Am 1974;64:798–803.
[9] Cai QM, Liou KN. Polarized light scattering by hexagonal ice crystals: theory. Appl Opt 1982;21:3569–80.
[10] Takano Y, Asano S. Fraunhofer diffraction by ice crystals suspended in the atmosphere. J Meteorol Soc Jpn 1983;61:289–300.
[11] Liou KN, Cai QM, Pollack JB, Cuzzi JN. Light scattering by randomly oriented cubes and parallelepipeds. Appl Opt 1983;22:3001–8.
[12] Takano Y, Liou KN. Solar radiative transfer in cirrus clouds. Part I: single-scattering and optical properties of hexagonal ice crystals. J Atmos Sci 1989;46:3–19.
[13] Parviainen P, Bohren CF, Mäkelä V. Vertical elliptical coronas caused by pollen. Appl Opt 1994;33:4548–51.
[14] Tränkle E, Mielke B. Simulation and analysis of pollen coronas. Appl Opt 1994;33:4552–62.
[15] Bi L, Yang P, Kattawar GW, Hu Y, Baum BA. Diffraction and external reflection by dielectric faceted particles. J Quant Spectrosc Radiat Transfer 2011;112:163–73.
[16] Hesse E, Macke A, Havemann S, Baran AJ, Ulanowski Z, Kaye PH. Modelling diffraction by facetted particles. J Quant Spectrosc Radiat Transfer 2012;113:342–7.
[17] Liou KN. In: An introduction to atmospheric radiation. 2nd ed San Diego: Academic Press; 2002.